Marco Agus
magus@crs4.it

Andrea Giachetti
giach@crs4.it

Enrico Gobbetti
gobbetti@crs4.it

Gianluigi Zanetti
zag@crs4.it

Antonio Zorcolo
zarco@crs4.it
CRS4
VI Strada Ovest
Z. I. Macchiareddu
I-09010 Uta (CA), Italy
www.crs4.it

Real-Time Haptic and Visual Simulation of Bone Dissection

Abstract

Bone dissection is an important component of many surgical procedures. In this paper, we discuss a haptic and visual simulation of a bone-cutting burr that is being developed as a component of a training system for temporal bone surgery. We use a physically motivated model to describe the burr-bone interaction, which includes haptic forces evaluation, the bone erosion process, and the resulting debris. The current implementation, directly operating on a voxel discretization of patient-specific 3D CT and MR imaging data, is efficient enough to provide real-time feedback on a low-end multiprocessing PC platform.

1 Introduction

Bone dissection is an important component of many surgical procedures. In this paper, we discuss a real-time haptic and visual implementation of a bone-cutting burr that is being developed as a component of a training simulator for temporal bone surgery. The specific target of the simulator is mastoidectomy, a very common operative procedure that consists in the removal, by use of the burring tool, of the mastoid portion of the temporal bone. The importance of computerized tools to support surgical training for this kind of intervention has been recognized by a number of groups that are currently developing virtual reality simulators for temporal bone surgery (Wiet et al., 2000; Pflesser, Petersik, Tiede, Hohne, & Leuwer, 2000). Our work is characterized by the use of patient-specific volumetric object models directly derived from 3D CT and MRI images, and by a design that provides realistic visual and haptic feedback, including secondary effects such as the obscuring of the operational site due to the accumulation of bone dust and other burring debris. The need to provide real-time feedback to users while simulating burring and related secondary effects imposes stringent performance constraints. Our solution is based on a volumetric representation of the scene, and it harnesses the locality of the physical system evolution to model the system as a collection of loosely coupled components running in parallel on a multiprocessor PC platform. Previous work has demonstrated the effectiveness of voxel-based representations for the generation of force feedback in the case of rigid body environments (McNeely, Puterbaugh, & Troy, 1999), virtual clay models (Avila & Sobierajski, 1996; Galyean & Hughes, 1991; Wang & Kaufman, 1995; He & Kaufman, 1997), or deformable bodies (Cotin, Delingette, & Ayache, 1996; Gibson et al., 1998; Frisken-Gibson, 1999; James & Pai, 2001).

This article, an extended version of our IEEE Virtual Reality 2002 contribution (Agus, Giachetti, Gobbetti, Zanetti, & Zorcolo, 2002a), focuses on the

modeling of the haptic and visual effects of bone bur-ring. We refer the reader to Agus, Giachetti, Gobbetti, Zanetti, and Zorcolo (2002b) for details on the other system components.

In our model, the burr bit is represented by a re-gion of space that samples the volumetric bone data to construct the elastic reaction and friction forces that the bone opposes to the burring. The sampling algorithm is similar in spirit to the Voxmap Point-Shell approach (McNeely et al., 1999), even though here we use a volumetric region around the burr to select the bone voxels relevant to force calculation. Our algorithm for computing forces, loosely pat-terned on Hertz contact theory (Landau & Lifshitz, 1986), is robust and a smooth function of the burr position. The computed forces are transfered to the haptic device via a sample-estimate-hold (Ellis, Sarkar, & Jenkins, 1997) interface to stabilize the system. Bone erosion is modeled by postulating an energy balance between the mechanical work per-formed by the burr motor and the energy needed to cut the bone; it is assumed to be proportional to the bone mass removed. The actual bone erosion is im-plemented by decreasing the density of the voxels that are in contact with the burr in a manner that is consistent with the predicted local mass flows. The process of accumulation of bone dust and other bur-ring debris are then handled using a particle system simulation based on simple, localized, sandpile mod-els. The resulting bone dissection simulator provides haptic and visual renderings that are considered suffi-cient for training purposes.

The rest of the paper is structured as follows. Section 2 provides a brief description of the application area, and section 3 is dedicated to the bone-burr interaction model. Section 4 describes how bone dust, debris, and water are simulated. Section 5 is devoted to the tech-niques used to provide real-time visual rendering in par-allel to the simulation. Section 6 outlines how rendering and simulation are integrated in the training system. Implementation details and results are reported in sec-tion 7. Finally, section 8 reports on conclusions and future work.

2   Application Area: Mastoidectomy

Mastoidectomy consists of the removal of the air cavities just under the skin behind the ear. (See figure 1.) It is the most superficial and common surgery of the temporal bone, and it is performed for chronic infection of the mastoid air cells (mastoiditis). The mastoid air cells are widely variant in their anatomy, and the main risks of the procedure are related to the detection and avoidance of the facial nerve, venous sinuses, and "dura mater."

In the typical mastoidectomy surgical setup, the sur-geon looks at the region affected by the procedure via a stereoscopic microscope and holds in her hands a high-speed burr and a sucker that she uses, respectively, to cut the bone and to remove water (used to cool the burr bit) and bone paste produced by the mixing of bone dust with water. (See figure 2a.) Subjective analy-sis of video records, together with in situ observations (Agus et al., 2002), highlighted a correlation between burring behaviors and type and depth of bone. In the case of initial cortex burring, burr tip motions of ap-proximately 0.8 cm together with sweeps over 2–4 cm were evident. Shorter (1–2 cm) motions with rapid lat-eral strokes characterized the postcortex mastoidectomy. For deeper burring, 1 cm strokes down to 1 mm were evident with more of a polishing motion quality, guided using the contours from prior burring procedures. The typical sweeping movement speed is of about 1 mm/ sec. Static burr handling was also noted, eroding bone tissue while maintaining minimal surface pressure.

The procedure requires bimanual input, with high-quality force feedback for the dominant hand (control-ling the burr/irrigator) and only collision detection for the nondominant one (controlling the sucker). Visual feedback requires a microscope-like device with at least four DOF.

The capability of replicating the effects caused by the intertwining of the different physical processes is of pri-mary importance for training (John et al., 2001; Agus et al., 2002). Although the presence of the water/bone paste mixture is essentially irrelevant with respect to the interaction between the burr and the bone, its presence cannot be neglected in the creation of the visual feed-
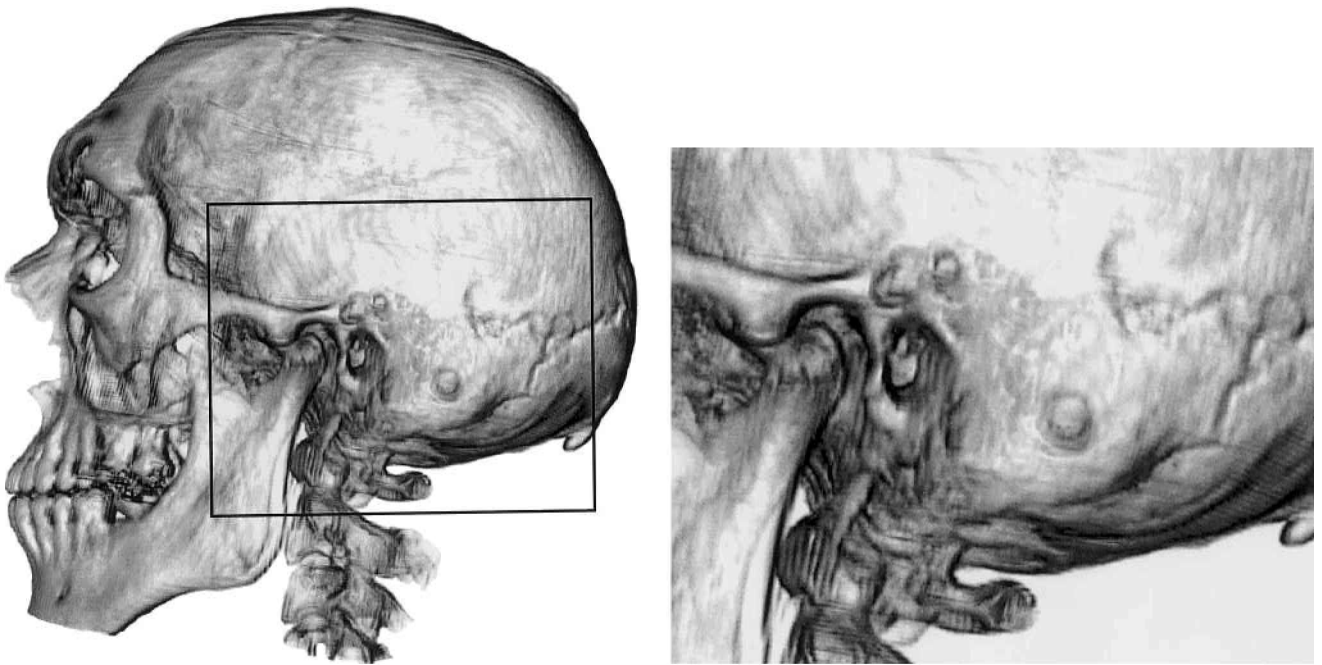
Figure 1. *Surgical site. Mastoidectomy is performed in the region indicated by the rectangle in (a) and zoomed in (b). The images are taken directly from the volumetric renderer used in the simulator. The volumetric data set has a resolution of 256 × 256 × 219 voxels and is derived from The Visible Human Male CT data set made available by The National Library of Medicine.*

back, because its obscuring effects constitute the principal cue to the user for the use of the suction device. (See figure 2.)

3 Bone-Burr Interaction Model

A detailed mechanical description of a rotating burr-cutting bone is complicated because it involves tracking the continuously changing free surface of the material being cut, the impact of the burr blades on the surface, the resulting stress distribution in the material, and the consequent plastic deformation and breakup.

To circumvent these complications, we have divided the cutting process into two successive steps. The first step estimates the bone material deformation and the resulting elastic forces, given the relative position of the burr with respect to the bone. For efficiency reasons, we currently do not simulate in this first step the high frequencies due to the high-speed contact between burr

bit blades and bone. This is, in our opinion, a minor limitation of the model because human tactile sensing is limited, except for very fine feature recognition tasks, to 400 Hz bandwidth (Shimoga, 1992). The second step estimates the local rate of cutting of the bone by using an energy balance between the mechanical work performed by the burr motor and the energy needed to cut the bone, and it is assumed to be proportional to the bone mass removed.

We will first describe this approach on a continuum model and then specialize the results to a discretized voxel grid.

3.1 Continuum Description

3.1.1 Forces Evaluation. Figure 3 illustrates an idealized version of the impact of burr on bone. The burr has a spherical bit, of radius R, that is rotating with angular velocity, $\vec{\omega}$. At time step, t, the burr is just outside the bone material, while at the next time step it is
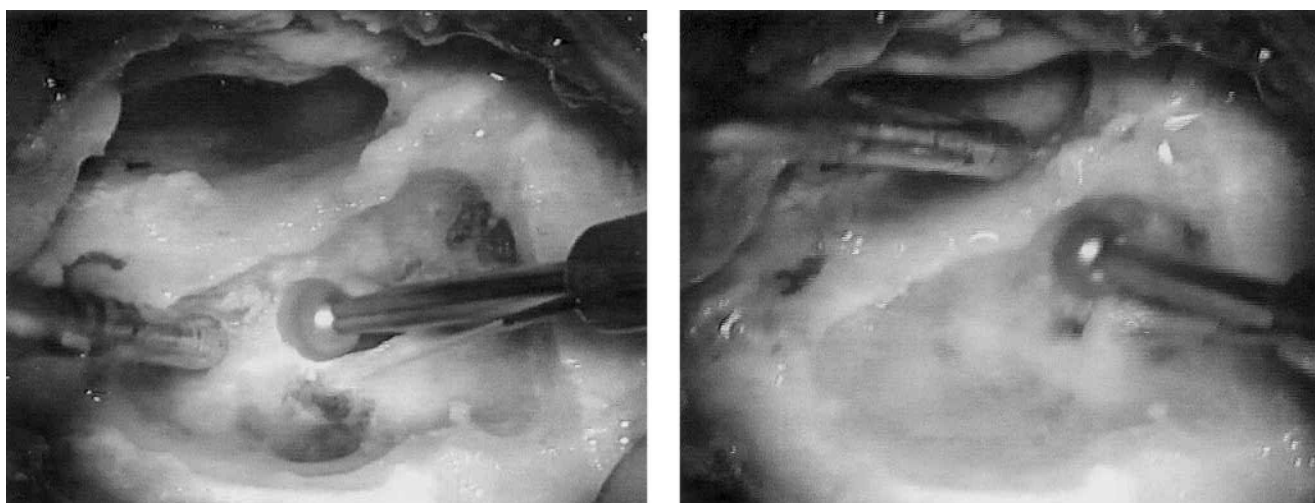
Figure 2. *Operation scene. These two images are typical examples of what is seen by the surgeon while performing a mastoidectomy. In (a), the paste created by the mixing of bone dust with water is clearly visible. If the paste and the water are not removed, they can obscure the field of view (b). Photos courtesy of Prof. Stefano Sellari Franceschini, ENT Surgery, Dept. of Neuroscience, University of Pisa.*
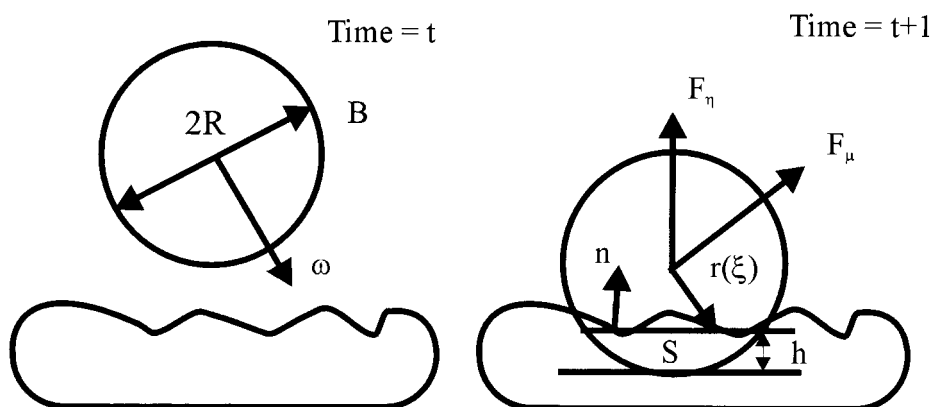

Figure 3. *The impact of burr on bone. Here we represent two successive instants, at time* t *and* t + 1, *of an idealized version of a surgeon burr. The burr has a spherical bit, of radius* R, *that is rotating with angular velocity* $\vec{\omega}$. *The surface* S *is the effective contact surface between the burr and the bone.*

intersecting the bone surface. In the following, we will refer to the sphere representing the burr bit as *B*, and to the contact surface between the burr and the bone as *S*.

All the relevant geometrical information is contained in the volumetric distribution of the bone material. We use a characteristic function, $\chi(\vec{r})$, to indicate the presence/absence of bone, where $\vec{r}$ is measured from the center of *B*. The first two moments of χ, restricted to the region contained in *B* are, respectively,

$$M = \int_{r<R} dr^3 \chi(\vec{r}) , \qquad (1)$$

$$\vec{M}_1 = \int_{r<R} dr^3 \chi(\vec{r}) \vec{r}. \tag{2}$$

We can now estimate the normal direction, $\hat{n}$, to S, as $\hat{n} = -\vec{M}_1/|M_1|$ and the "thickness" h of B immersed in the bone, by solving $M = \pi h^2(R - h/3)$. We can now derive, assuming that $h/R << 1$, and using Hertz's contact theory (Landau & Lifshitz, 1986), an expression for the total force, $\vec{F}_e$, exerted on the burr by the elastic deformation of the bone:

$$\vec{F}_e = C_1 R^2 \left(\frac{h}{R}\right)^{3/2} \hat{n}, \tag{3}$$

where C_1 is a dimensional constant that describes the elastic properties of the material. Moreover, we can give an expression for the pressure, $\vec{P}(\vec{\xi})$, exerted by the burr on the point $\vec{\xi}$ of S:

$$\vec{P}(\vec{\xi}) = -\frac{3}{2\pi a^2} \sqrt{1 - \frac{|\vec{\xi}|^2}{a^2}} \vec{F}_e, \tag{4}$$

where $\vec{\xi}$ is measured from the center of S (see figure 3b), and a is the radius of the contact region. In Hertz's contact theory, a can be estimated as

$$a = (C_1 R)^{1/3} F_e^{1/3}. \tag{5}$$

From equation (4), we can estimate the frictional force, $\vec{F}_\mu$, that the bone will oppose the burr rotation:

$$\vec{F}_\mu = \mu \int_{\xi<a} d\sigma P(\vec{\xi}) \frac{\vec{r}(\vec{\xi}) \times \vec{\omega}}{|\vec{r}(\vec{\xi})||\vec{\omega}|}, \tag{6}$$

where μ is a friction coefficient that links the frictional forces for unit area to the locally exerted pressure.

The total force that should be returned by the haptic feedback device is, therefore, $\vec{F}_T = \vec{F}_e + \vec{F}_\mu$.

3.1.2 Erosion Modeling.

We assume that all the power spent by working against frictional forces goes toward the erosion of the bone material. In other words, we equate for each contact surface element $d\sigma$

$$\mu P(\vec{\xi}) \omega r(\vec{\xi}) \left(1 - \left(\frac{\vec{r}(\vec{\xi}) \cdot \vec{\omega}}{|\vec{r}(\vec{\xi})||\vec{\omega}|}\right)^2\right) d\sigma = \alpha \phi(\vec{\xi}) d\sigma, \tag{7}$$

where α is a dimensional constant and $\phi(\vec{\xi})$ is the mass flux at the contact surface point $\vec{\xi}$. Using the mass flux, ϕ, one can update the position of the bone surface.

These formulas have been written with the implicit assumption that the burr blades are very small with respect to the burr bit radius and that their effect can be absorbed in the friction constant, μ, and in the erosion constant, α. Even though this is, in general, false, and Hertz's theory is, strictly speaking, valid for only small elastic deformations, this formulation provides a computationally tractable, robust expression for the response forces that, at least in the limit of small h, is physically reasonable.

3.2 Discretized Description

3.2.1 Forces Evaluation.
In the simulator, the bone distribution is known only at the level of a volumetric grid discretized in cubic voxels. Equation (1), (2), and (6) need, therefore, to be translated and reinterpreted.

A direct translation will transform integrals in sums over the voxels that have non-null intersection with B. The evaluation of each voxel contribution is computationally complex because it requires finding the intersections between B and the cube defining the voxel. To simplify matters, we are approximating the voxels with spheres of the same volume, centered at the voxel center, $\vec{c}_i$, with the origin at the center of B. The radius of the voxel spheres, η, is, therefore, defined by $4/3 \pi \eta^3 = l^3$, where l is the length of the voxel side.

Using this approximation, it is trivial to derive simple formulas that express, in terms of the distance $d = |\vec{c}_i|$, the volume, ΔV, of the intersection region; the area, $\Delta\sigma$, of the intersection surface; and the actual distance, r, from the center of the intersection surface to the center of B. (See figure 4.)

$$\Delta v(d) = \frac{\pi}{12} \bigg(d^3 - 6(R^2 + \eta^2)d$$
$$+ 8(R^3 + \eta^3) - 3(\eta^2 - R^2)^2 \frac{1}{d} \bigg) \tag{8}$$
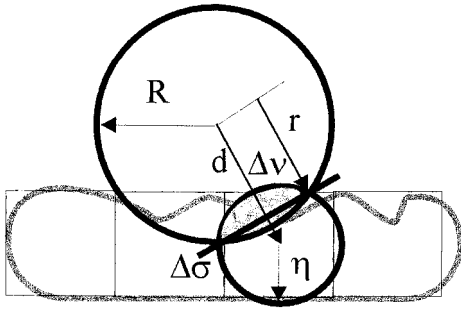
Figure 4. *Voxel approximation. To simplify computations, voxels are approximated with spheres of the same volume. In this way, simple formulas for volume and surface intersection can be derived.*

$$\Delta\sigma(d) = \frac{\pi}{4}\left(2(\eta^2 + R^2) - d^2 - (\eta^2 - R^2)^2\frac{1}{d^2}\right)$$

(9)

$$r(d) = \frac{1}{2}d + \frac{R^2 - \eta^2}{2}\frac{1}{d}$$

(10)

The required integrals then become

$$M^\star = \sum_i \Delta V(|\vec{c}_i|)\chi_i$$

(11)

and

$$\vec{M}_1^\star = \sum_i \Delta V(|\vec{c}_i|)\chi_i\frac{r_i}{d_i}\vec{c}_1 .$$

(12)

To estimate the friction force, $\vec{F}_\mu$, we convert the area integral (6) in

$$\vec{F}_\mu = \mu\sum_i\Delta\sigma(|\vec{c}_i|)P(\vec{\xi}_i)\frac{\vec{c}_i \times \vec{\omega}}{|\vec{c}_i||\vec{\omega}|},$$

(13)

with

$$\vec{\xi}_i = \frac{r_i}{d_i}\left(\vec{c}_i - \frac{(\vec{\omega} \cdot \vec{c}_i)}{\omega^2}\vec{\omega}\right) .$$

(14)

The power spent by the frictional forces on a voxel is then

$$\mu P(\xi_i)\omega r_i(\vec{\xi}_i)\left(1 - \left(\frac{\vec{c}_i \cdot \vec{\omega}}{|\vec{c}_i||\vec{\omega}|}\right)^2\right)\Delta\sigma_i = \alpha\phi_i\Delta\sigma_i ,$$

(15)

where ϕ_i is the mass flux per unit surface coming out of voxel i, via surface $\Delta\sigma_i$. To evaluate P, we use formula (4), where for a we use the "effective" radius of the contact surface $a^\star = \sqrt{2Rh - h^2}$.

3.2.2 Erosion Modeling. Using the fluxes, ϕ_i, we can now erode the voxels in the intersection region. In our current implementation, we associate an eight-bit counter with each voxel, representing the voxel density, and decrease it by a value proportional to the "assumed" amount of removed mass, $\Delta M_i = \Delta t\Delta\sigma\phi_i$, where Δt is the time step of the simulation, and the mass, M_i, contained in the voxel i. The bone material in the temporal bone area has a morphological structure that ranges from compact bone, such as close to the outer skull surface, to a porous, "trabecular" consistency. The porous scale ranges from a few millimeters down to scales well beyond the resolution of the medical imaging devices. In our model, the subscale modeling of the trabecular structures is absorbed in a voxel-dependent erosion constant α.

3.3 Sample-Estimate-Hold Interface

A direct transmission of the computed forces to the haptic device is, in the case of "almost rigid" contacts, usually plagued by mechanical instabilities. The typical solution for this problem is the introduction of an artificial, "virtual" coupling between the haptic device and the virtual environment (Colgate, 1994; Adams & Hannaford, 1999).

In our system, we use a sample-estimate-hold approach (Ellis et al., 1997) to remove the excess energy injected by the standard zero-order hold of force employed by the haptic device drivers. With this technique, we compute the force that is sent to the haptic device based on the previous zero-order representations produced at regular intervals by our burr-bone interaction model. This new value of force, when held over the corresponding sampling interval, approximates the force-time integral more closely than the usual zero-order hold (Ellis et al., 1997).

4   Bone Dust, Debris, and Water Simulation

We are modeling the dust/fluid dynamics using a hybrid particles-volumetric model, inspired by previous work on particle systems and sandpiles (Sumner, O'Brien, & Hodgins, 1999; Li & Moshell, 1993).

Each particle has a mass, a position, a velocity, and a dynamic behavior. Water particles are introduced by the irrigator with an initial velocity directed along the irrigator axis. Dust particles are generated by the burr performing the surgical bone drilling with an initial velocity depending on the rotation of the burr itself and a creation rate depending on the mass flux. Blood particles are generated by tissues with negligible initial speed. All particles move according to Newton's law when free, and interact with the other materials according to a set of rules that ensure that only a single particle may occupy a given voxel at a given time. Basically, when a particle enters a non-empty voxel, it is reflected backwards to the first free voxel. Its state is then modified as a function of the colliding materials and the particle velocity. When a particle collides with the environment, we choose between elastic scattering or sliding along the bone surface based on the particle velocity. The random choice is made according to a probability distribution that favors scattering for high-impact velocities. Different materials are modeled by shaping the probability distribution and by defining different particle masses and reflection coefficients. In particular, bone particles have a behavior similar to water, but higher mass and higher probability to be scattered by hard bone.

We model bone paste formation by changing the material of bone and water particles to "bone paste" when they collide. We also consider the interaction of particles with the burr by scattering away the particles that enter in contact with the burr bit with a velocity depending on the rotational axis and speed of the burr.

5   Real-Time Visual Rendering

The state of the simulation is entirely described by the contents of the rectilinear grid that contains the material labels used in the simulation. This also includes the particles modeling bone dust, debris, and water. We provide real-time visual feedback in parallel with the simulation of the physical system with a direct volume-rendering approach. Rendering such a dynamic volume under real-time constraints is particularly challenging. In our approach, a fast approximation of the diffuse shading equation (Max, 1995) is computed on the fly by the graphics pipeline directly from the scalar data. We do this by exploiting the possibilities offered by multi-texturing with the register combiner OpenGL extension that provides a configurable means to determine per-pixel fragment coloring (Kilgard, 2001). The extension is available on commodity graphics boards (such as the NVIDIA GeForce series).

Object-aligned volume slices are composed back to front. The Lambert shading equation is implemented in the graphics hardware by programming the register combiners, using multi-texturing to compute intermediate slices and approximate opacity gradients with forward differences. Gradient norms, that provide "surface strength" (Drebin, Carpenter, & Hanrahan, 1988), are computed using a second-order approximation of the square root programmed with the register combiners. We refer the reader to Agus et al. (2002b) for more detail on the rendering technique.

This procedure is extremely efficient because all the computation is performed in parallel in the graphics hardware and no particular synchronization is needed between the renderer and the process that is modifying the data set. Only a single sweep through the volume is needed, and volume slices are sequentially loaded into texture memory on current standard PC graphics platform using AGP 4$\times$ transfers, which provide a peak bandwidth of 1054 MB/sec.
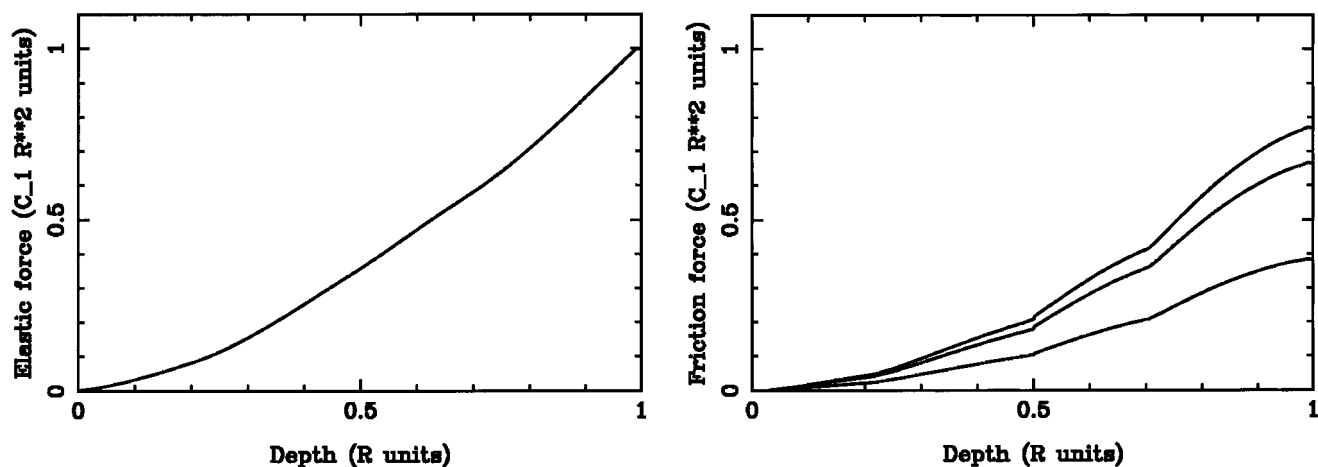
Figure 5. *Virtual bone reaction against burr penetration. The computations are done in absence of erosion, $\alpha = \infty$, using the actual force evaluation kernel of the force feedback loop. In (a), we show the "elastic" response of the material, measured in units of $C_1 R^2$, as a function of the burr tip penetration depth in units of the burr bit radius R. Figure (b) illustrates the "frictional" response of the material, with $\mu = 1/2$ and for different angles θ, $\theta = 30, 60,$ and 90 deg. between the surface normal and $\vec{\omega}$. The strength of F_μ increases for increasing $\sin(\theta)$. The knees in the F_μ curves correspond to the intersection of the burr bit with a deeper bone voxel layer.*

6   System Integration

Our technique for bone dissection simulation has been integrated in a prototype training system for mastoidectomy. We have exploited the difference in complexity and frequency requirements of the visual and haptic simulations by modeling the system as a collection of loosely coupled concurrent components. Logically, the system is divided in a "fast" subsystem, responsible for the high-frequency tasks (surgical instrument tracking, force feedback computation, and bone erosion), and a "slow" one, which is essentially dedicated to the production of data for visual feedback. The slow subsystem is responsible for the global evolution of the water, bone dust, and bone paste. The algorithms used to control the simulations are local in character, and they are structured so that they communicate only via changes in the relevant, local, substance densities. This arrangement leads naturally to a further breakup of the slow subsystem in components, each dedicated to the generation of a specific visual effect, and thus to a parallel implementation on a multiprocessor architecture. The system runs on two interconnected

multiprocessor machines, and the data is initially replicated on the two machines. The first is dedicated to the high-frequency tasks: haptic device handling and bone removal simulation, which run at 1 kHz. The second concurrently runs, at about 15–20 Hz, the low-frequency tasks: bone removal, fluid evolution, and visual feedback. Because the low-frequency tasks do not influence the high-frequency ones, the two machines are synchronized using one-way message passing, with a dead-reckoning protocol to reduce communication bandwidth.

7   Implementation and Results

Our current configuration is as follows (see figure 5):

- a single-processor PII/600 MHz with 256 MB PC133 RAM for the high-frequency tasks; two threads run in parallel: one for the haptic loop (1 kHz) and one for sending volume and instruments position updates to the other machine;
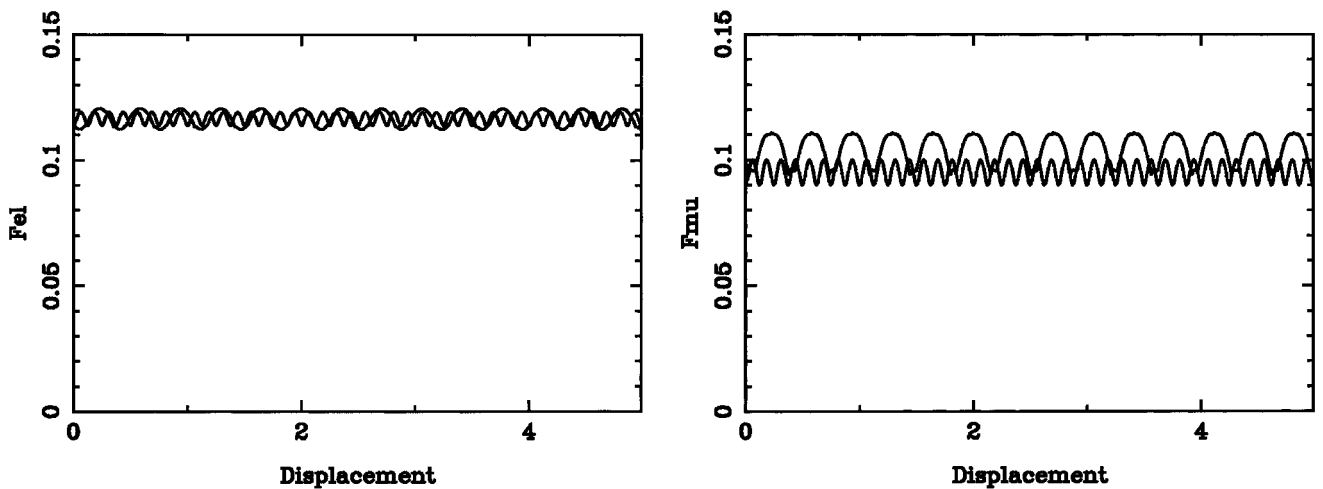
Figure 6. *Sliding motion, constrained experiment. The reaction of the flat surface of virtual bone to the sliding motion of a burr bit immersed at a depth of R/4. Figure (a,b) show, respectively, the "elastic" and the "frictional" force response of the material, measured in units of C_1R^2, as a function of the distance traveled along the plane measured in R units. The pair of curves in each figure correspond to a sliding motion over a bone surface aligned along, respectively, one of the voxel discretization axis, and a plane with normal $\left[0, \frac{1}{\sqrt{2}}, \frac{1}{\sqrt{2}}\right]$. The fluctuations in the force values are due to the "voxel sphere" approximation used to compute F. The difference in the wavelength of the fluctuations is a factor of $\sqrt{2}$ as expected.*

- a dual-processor PIII/600 MHz with 512 MB PC800 RAM and a NVIDIA GeForce 3 Ti 500 and running a 2.4 linux kernel for the low-frequency tasks; three threads are continuously running on this machine: one to receive volume and position updates, one to simulate bone removal and fluid evolution, and one for visual rendering;
- a PHANToM desktop haptic device for the dominant hand; the device is connected to the single processor PC. It provides six-DOF tracking and three-DOF force feedback for the burr/irrigator;
- a PHANToM 1.0 haptic device for the nondominant hand; the device is connected to the single-processor PC. It provides six-DOF tracking and three-DOF force feedback for the sucker; and
- an n-vision VB30 binocular display for presenting images to the user; the binoculars are connected to the S-VGA output of the dual processor PC.

The performance of the prototype is sufficient to meet timing constraints for display and force feedback, even though the computational and visualization platform is constructed from affordable and widely accessi-ble components. We are currently using a volume of $256 \times 256 \times 128$ cubical voxels (0.3 mm side) to represent the region where the operation takes place. The force feedback loop is running at 1 kHz using a $5 \times 5 \times 5$ grid around the tip of the instruments for force computations. The computation needed for force evaluation and bone erosion takes typically $20\mu s$, and less than $200\mu s$ in the worst-case configuration.

In the following subsections, we will report on a series of experiments done using the prototype just described.

7.1 Force Evaluation

Figure 6 shows the reaction of the virtual bone against burr penetration. The computations are done in absence of erosion, $\alpha = \infty$, and using the actual force evaluation kernel of the force feedback loop.

Figure 6a illustrates the "elastic" response of the material, measured in units of C_1R^2, as a function of the burr tip penetration depth measured in units of the burr bit radius, R. Figure 6b illustrates the "frictional" re-
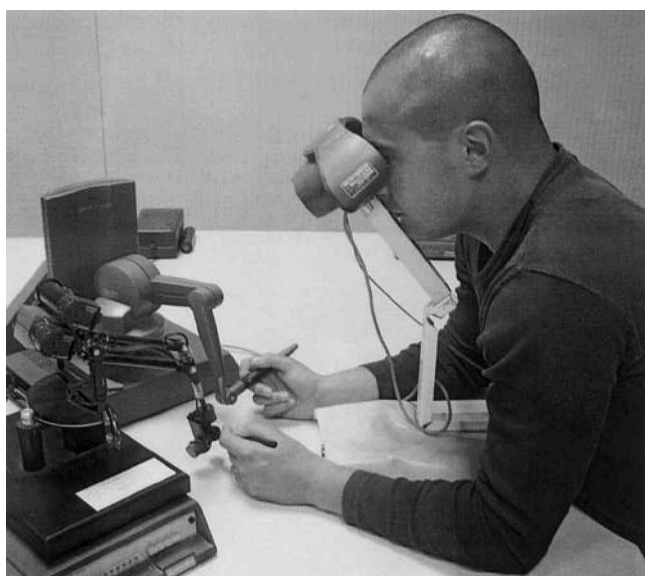
Figure 7. *The virtual surgical setup.*

Figure 7 shows the reaction of the virtual bone, again in runs with $\alpha = \infty$, to a sliding motion of the burr bit, immersed at a depth of $R/4$, over a flat bone surface. Figure 7 (a,b) shows, respectively, the "elastic" and the "frictional" force response of the material, measured in units of $C_1 R^2$, as a function of the distance traveled along the plane measured in R units. The pair of curves in each figure correspond to a sliding motion over a bone surface aligned along, respectively, one of the voxel discretization axis and a plane with normal $\left[0, \frac{1}{\sqrt{2}}, \frac{1}{\sqrt{2}}\right]$. The fluctuations in the force values are due to the "voxel sphere" approximation used to compute F. The difference in the wavelength of the fluctuations is a factor of $\sqrt{2}$ as expected.

7.2 Bone Erosion

Figure 8 illustrates a "freehand" experiment where bone is eroded by a polishing movement. The movement is similar to the one described in the previous subsection, with a sliding speed of about 10 mm/sec., and $\alpha = 3.1 \times 10^6$ mm^2/sec^2. Figure 8a shows the depth of the burr below the surface level as a function of time, and figure 8b reports the components of the force con-
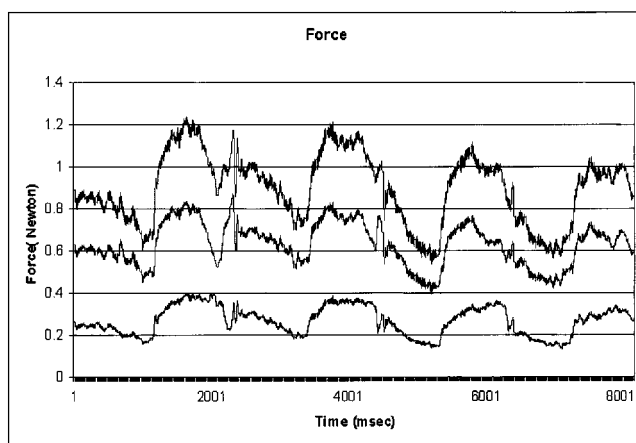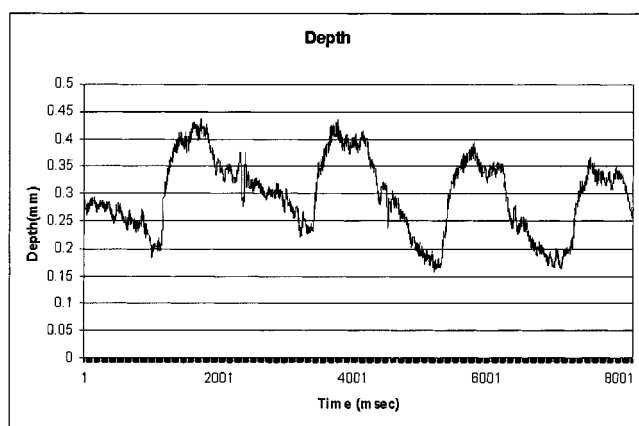
sponse of the material, with $\mu = 1/2$ and for different angles θ, $\theta = 30, 60$, and 90 deg., between the surface normal and $\vec{\omega}$. The strength of F_μ increases for increasing $\sin(\theta)$. The knees in the F_μ curves correspond to the intersection of the burr bit with a deeper bone voxel layer.

Figure 8. *Bone erosion, polishing movement. A "freehand" experiment in which bone is eroded by a polishing movement. The sliding speed is about 10 mm/sec., and $\alpha = 3.1 \times 10^6$ mm^2/sec^2. Figure (a) shows the depth of the burr below the surface level as a function of time. Figure (b) reports the components of the force contributions and the total force applied to the haptic display during the movement. The lower line is the friction force $\vec{F}_\mu$, the middle line is the elastic force $\vec{F}_{el}$, and the upper line is the total force $\vec{F}_{tot}$.*
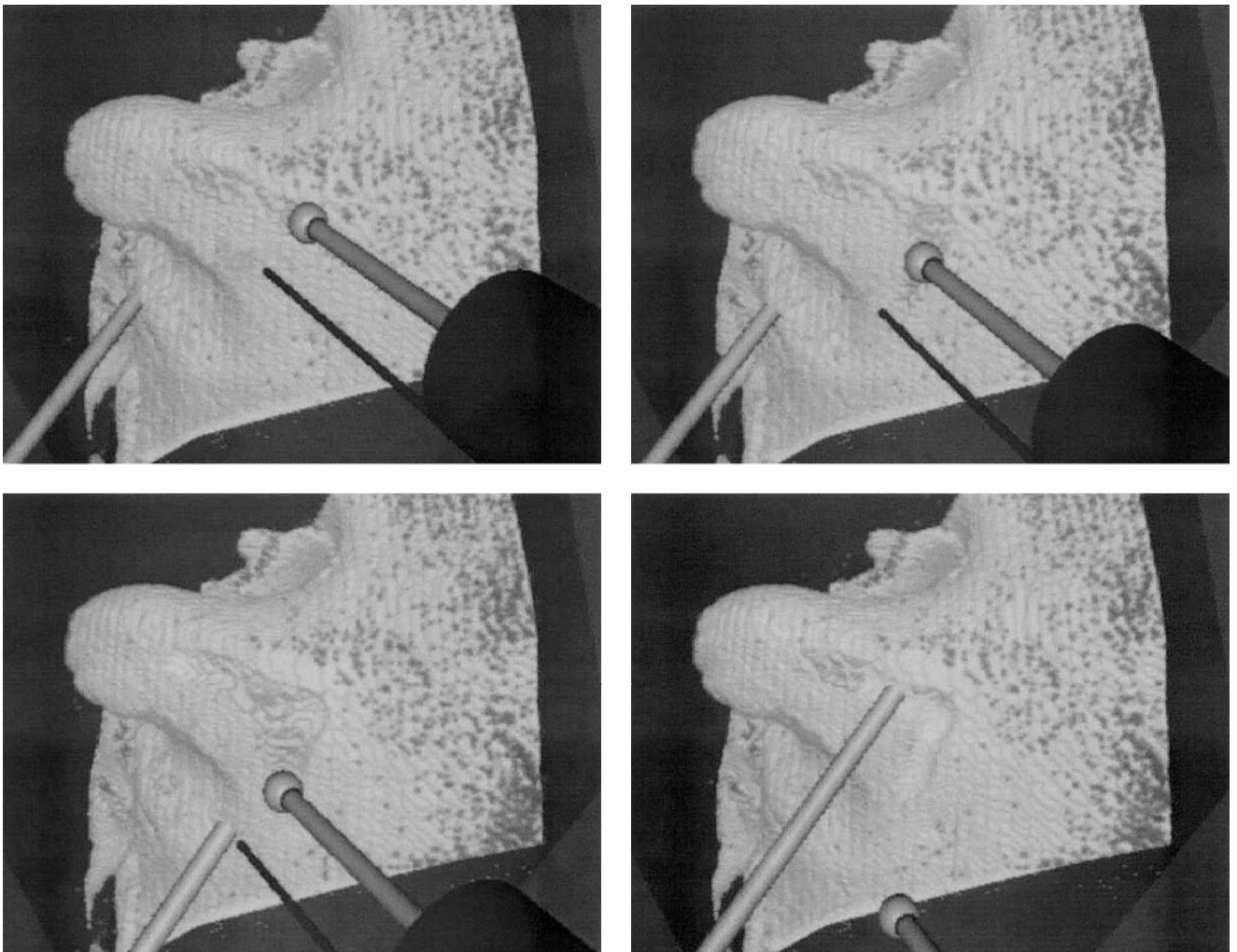
Figure 9. *A virtual burring sequence. Here we show a typical bone cutting sequence performed in the mastoid region. The accumulation of debris, and its masking effects, is clearly visible.*

tributions and the total force applied to the haptic display during the movement.

We have gathered initial feedback about the prototype system from specialist surgeons from the University of Pisa who are collaborating with us in this research. Subjective input is being used to tune the parameters that control force feedback, but the overall realism of the simulation is considered sufficient for training purposes. Figure 9 shows a typical erosion sequence, and a demonstration movie is available on the IERAPSI project Web site (Agus et al., 2001).

8 Conclusions and Future Work

We have presented a physically motivated haptic and visual implementation of a bone-cutting burr that is being developed as a component of a training system for temporal bone surgery. The current implementation, directly operating on a voxel discretization of patient-specific 3D CT and MR imaging data, is efficient enough to provide real-time multimodal feedback on a low-end multiprocessing PC platform. To further improve the efficiency of the simulation, we are currently

working on evaluating interaction forces using hierarchical techniques.

While subjective input from selected users is encouraging, it would be of extreme interest to compare our results with direct forces measurements obtained by drilling actual samples. Because, to our knowledge, there are no available data on the subject in literature, we are currently defining an experimental setup and measurement procedures.

In our simulator, we are currently using data sets that have the same resolution as the original medical imaging data, and we are not differentiating between compact and trabecular bone. It is our intention to explore the possibility of running the simulator on synthetically refined data sets obtained by using subvoxel trabecular bone modeling.

Acknowledgments

References

Adams, R., & Hannaford, B. (1999). Stable haptic interaction with virtual environments. *IEEE Transactions on Robotics and Automation, 15*(3), 465–474.

Agus, M., Bettio, F., Giachetti, A., Gobbetti, E., Zanetti, G., & Zorcolo, A. (2001). *Real-time haptic and visual simulation of bone dissection.* Video demonstration. [Online. Available at: http://www.crs4.it/ierapsi.]

Agus, M., Giachetti, A., Gobbetti, E., Zanetti, G., John, N. W., & Stone, R. J. (2002). Mastoidectomy simulation with combined visual and haptic feedback. In J. D. Westwood, H. M. Hoffmann, G. T. Mogel, & D. Stredney (Eds.), *Medicine meets virtual reality 2002* (pp. 17–23). Amsterdam: IOS Press.

Agus, M., Giachetti, A., Gobbetti, E., Zanetti, G., & Zorcolo, A. (2002a). Real-time haptic and visual simulation of bone dissection. In *IEEE Virtual Reality Conference,* 209–216.

——— (2002b). A multiprocessor decoupled system for the simulation of temporal bone surgery. *Computing and Visualization in Science, 5*(1), 35–43.

Avila, R. S., & Sobierajski, L. M. (1996). A haptic interaction method for volume visualization. *Proceedings of the Conference on Visualization '96,* 197–204.

Colgate, J. (1994). Issues in the haptic display of tool use. *Proceedings of ASME Haptic Interfaces for Virtual Environment and Teleoperator Systems,* 140–144.

Cotin, S., Delingette, H., & Ayache, N. (1996). Real time volumetric deformable models for surgery simulation. *VBC,* 535–540.

Drebin, R. A., Carpenter, L., & Hanrahan, P. (1988). Volume rendering. *Computer Graphics, 22*(4), 51–58.

Ellis, R., Sarkar, N., & Jenkins, M. (1997). Numerical methods for the force reflection of contact. *ASME Transactions on Dynamic Systems, Modeling, and Control, 119*(4), 768–774.

Frisken-Gibson, S. F. (1999). Using linked volumes to model object collisions, deformation, cutting, carving, and joining. *IEEE Transactions on Visualization and Computer Graphics, 5*(4), 333–348.

Galyean, T. A., & Hughes, J. F. (1991). Sculpting: an interactive volumetric modeling technique. *Proceedings of the 18th annual conference on computer graphics and interactive techniques,* 267–274.

Gibson, S., Fyock, C., Grimson, E., Kanade, T., Kikinis, R., Lauer, H., McKenzie, N., Mor, A., Nakajima, S., Ohkami, H., Osborne, R., Samosky, J., & Sawada, A. (1998). Volumetric object modeling for surgical simulation. *Medical Image Analysis, 2*(2), 121–132.

He, T., & Kaufman, A. (1997). Collision detection for volumetric objects. In *Proceedings of the Conference on Visualization '97,* 27-ff.

James, D., & Pai, D. (2001). A unified treatment of elastostatic contact simulation for real time haptics. *Haptics-e, The Electronic Journal of Haptics Research, 2*(1), 1–13.

John, N. W., Thacker, N., Pokric, M., Jackson, A., Zanetti, G., Gobbetti, E., Giachetti, A., Stone, R. J., Campos, J., Emmen, A., Schwerdtner, A., Neri, E., Franceschini, S. S., & Rubio, F. (2001). An integrated simulator for surgery of the petrous bone. In J. D. Westwood (Ed.), *Medicine meets virtual reality 2001* (pp. 218–224). Amsterdam: IOS Press.

Kilgard, M. J. (Ed.). (2001). *NVIDIA OpenGL extension specifications.* NVIDIA Corporation.

Landau, L., & Lifshitz, E. (1986). *Theory of elasticity.* Oxford: Pergamon Press.

Li, X., & Moshell, J. (1993). Modeling soil: Realtime dynamic models for soil slippage and manipulation. *Computer Graphics Proceedings, Annual Conference Series,* 361–368.

Max, N. (1995). Optical models for direct volume rendering. *IEEE Transactions on Visualization and Computer Graphics, 1*(2), 99–108.

McNeely, W. A., Puterbaugh, K. D., & Troy, J. J. (1999). Six degrees-of-freedom haptic rendering using voxel sampling. In A. Rockwood (Ed.), *SIGGRAPH 1999* (pp. 401–408). Los Angeles: Addison Wesley Longman.

Pflesser, B., Petersik, A., Tiede, U., Hohne, K. H., & Leuwer, R. (2000). Volume based planning and rehearsal of surgical interventions. In Lemke, H. U., et al. (Ed.), *Computer assisted radiology and surgery, proc. CARS 2000, excerpta medica international congress* (pp. 607–612). Amsterdam: Elsevier.

Shimoga, K. (1992). Finger force and touch feedback issues in dextrous telemanipulation. *Proceedings of NASA-CIRSSE International Conference on Intelligent Robotic Systems for Space Exploration.,* 159–178.

Sumner, R., O'Brien, J., & Hodgins, J. (1999). Animating sand, mud and snow. *Computer Graphics Forum, 18,*(1), 17–26

Wang, S. W., & Kaufman, A. E. (1995). Volume sculpting. *Proceedings of the 1995 Symposium on Interactive 3D Graphics,* 151-ff.

Wiet, G., Bryan, J., Sessanna, D., Streadney, D., Schmalbrock, P., & Welling, B. (2000). Virtual temporal bone dissection simulation. In J. D. Westwood (Ed.), *Medicine meets virtual reality 2000* (pp. 378–384). Amsterdam: IOS Press.